Hybrid Lattice Boltzmann Method on overlapping grids

G. Di Ilio,[1,*] D. Chiappini,[2] S. Ubertini,[3] G. Bella,[4] and S. Succi[5]

[1] *University of Naples 'Parthenope', Centro Direzionale Isola C4, 80133 Naples, Italy*
[2] *University of Rome 'Niccolò Cusano', Via don Carlo Gnocchi 3, 00166, Rome, Italy*
[3] *University of Tuscia, Largo dell'Università snc, 01100, Viterbo, Italy*
[4] *University of Rome 'Tor Vergata', Via del Politecnico 1, 00133, Rome, Italy*
[5] *Istituto Applicazioni Calcolo, CNR, Via dei Taurini 19, 00185, Rome, Italy*

(Dated: December 29, 2016)

In this work, an Hybrid Lattice Boltzmann Method (HLBM) is proposed, where the standard Lattice Boltzmann implementation based on the Bhatnagar-Gross-Krook (LBGK) approximation is combined together with an Unstructured finite-volume Lattice Boltzmann (ULBE) model. The method is constructed on an overlapping grid system, which allows the coexistence of a uniform lattice nodes spacing and a coordinate-free lattice structure.
The natural adaptivity of the hybrid grid system makes the method particularly suitable to handle problems involving complex geometries. Moreover, the provided scheme ensures high accuracy solution near walls, given the capability of the unstructured sub-model of achieving the desired level of refinement in a very flexible way. For these reasons, the HLBM represents a prospective tool for solving multi-scale problems.
The proposed method is here applied to the benchmark problem of a two-dimensional flow past a circular cylinder for a wide range of Reynolds numbers and its numerical performances are measured and compared with the standard LBGK ones.

PACS numbers: 47.11.Qr, 47.11.-j, 47.11.Df
Keywords: Hybrid Lattice Boltzmann Method ; grid refinement ; finite-volumes ; unstructured grids

I. INTRODUCTION

Within the last two decades, the Lattice Boltzmann (LB) method has gained a prominent role among the computational fluid dynamics approaches, providing an efficient tool for solving a wide class of fluid flow problems [1–4]. Recent developments in the LB research have lead to the formulation of advanced models which strongly enhanced the capability of this method. In particular, since the first original implementations [5, 6], much effort has been devoted to overcome the limit of the uniform lattice spacing.
Several finite-volume and finite-difference formulations for the LB technique are available in literature, which extend the method to non-uniform grids. The model of Nannelli and Succi [7] was the first to be proposed. Kandhai et al. [8] developed an approach based on multiple nested lattices with increasing resolution. Other important works are those of Peng et al. [9] and Xi et al. [10] who introduced the possibility of dealing with unstructured meshes. Quite recently, further developments of the unstructured Lattice Boltzmann method have been presented in [11–13]. Of particular interest for the present study is the work of some of the authors [14], which laid down the foundations of the unstructured sub-model employed in the hybrid scheme proposed here. A different approach to solve the Lattice Boltzmann equation on non-uniform and unstructured meshes is provided in [15–18]. In those studies, Galerkin-type finite element methods are developed.
Another possible strategy to extend the applicability of the LB method and improve its efficiency is the grid refinement. Such methods operate employing locally refined patches in those regions of the fluid domain where a higher resolution is required. Filippova and Hanel [19] introduced the first model together with a boundary-fitting scheme for curved geometries. In their work, the exchange of information between coarse and fine grids takes place in the post-collision step. A further improvement of such method is provided in [20], where an acceleration scheme based on the idea of using different molecular speeds on the fine grid and on the coarse grid is developed. Accurate and efficient approaches are also the multi-block methods provided by Lin and Lai [21] and Yu et al. [22]. Dupuis and Chopard [23] proposed an alternative and more general model in which the pre-collision distribution functions, rather then the post-collision ones, are rescaled according to the transformation rules between one grid and the other. More recently, Chen et al. [24] developed a grid refinement algorithm based on a volumetric formulation.
Despite the flexibility provided by unstructured models, such class of methods present a severe limitation, with respect to the standard LB method, concerning the computational efficiency. On the other hand, the discussed advanced refinement techniques for structured grids work remarkably well, but are still somehow limited in handling complex geometries, mainly due to the requirement of interpolation routines to calculate the fluid dynamic variables on the surface of the body.
In this work, we propose an hybrid Lattice Boltzmann scheme which couples a standard uniform grid model

* giovanni.diilio@uniparthenope.it

with an unstructured model. The new method combines the advantages of traditional and unstructured LB approaches, resulting in an accurate, flexible and efficient tool for fluid dynamic problem solutions. The hybrid method is then tested for the benchmark problem of a flow past a circular cylinder in two dimensions and its performance is evaluated in comparison with the standard LBGK method.

Here, we conduct a two-dimensional study only. However, we emphasize that an extension of the hybrid method to the three-dimensional case, although being practically laborious, is conceptually straightforward. In this work, we show the method for an unstructured mesh based on triangular element; nevertheless, the general approach does not depend on the type of element adopted. Thus, a generalization to other mesh discretization and, in particular, to the three-dimensional case, requires the implementation of an appropriate Lattice Boltzmann formulation for the unstructured model and different interpolation procedures. Extensions of the unstructured method are already present in literature [25]. Thus, the main concern is related to the implementation of interpolation schemes for three-dimensional interfaces.

II. METHODOLOGY

The proposed model combines the standard LBGK scheme with an unstructured finite-volume LB formulation. The fluid domain is composed of a uniformly spaced regular lattice structure together with an unstructured grid. The two conformed components overlap where they meet, completely covering the physical space of the domain. Both numerical schemes are built on the LB single-time relaxation approach, which is described by the following Lattice Boltzmann equation in differential form:

$$\frac{\partial f_i(\mathbf{x},t)}{\partial t}+\mathbf{c}_i\cdot\nabla f_i(\mathbf{x},t)=-\frac{1}{\tau}\left[f_i(\mathbf{x},t)-f_i^{eq}(\mathbf{x},t)\right], \quad (1)$$

where $\mathbf{x}$ represents the position of the particle in the discretized space at time t and $f_i(\mathbf{x},t)$ and $\mathbf{c}_i$ are the particle distribution functions and the set of discrete speeds, respectively, along the allowed lattice directions. In this formulation, the *collision operator* is here characterized by a single parameter, that is the *relaxation time* τ.

A. LBGK on uniform spaced discretized domain

The standard implementation scheme, which is solved on the regularly spaced discretized domain, is based on the explicit time differencing of equation (1) and is represented by the following relation:

$$f_i(\mathbf{x}+\mathbf{c}_i\Delta t_{\mathbf{s}},t+\Delta t_{\mathbf{s}})-f_i(\mathbf{x},t)= -\frac{\Delta t_{\mathbf{s}}}{\tau_{\mathbf{s}}}\left[f_i(\mathbf{x},t)-f_i^{eq}(\mathbf{x},t)\right], \quad (2)$$

where $\tau_{\mathbf{s}}$ and $\Delta t_{\mathbf{s}}$ are the relaxation time and the time step, respectively, for the 'structured' scheme and

$$f_i^{eq}(\mathbf{x},t)=w_i\rho(\mathbf{x},t)\left\{1+\frac{\mathbf{c}_i\cdot\mathbf{u}(\mathbf{x},t)}{c_s^2} +\frac{\left[\mathbf{c}_i\cdot\mathbf{u}(\mathbf{x},t)\right]^2}{2c_s^4}-\frac{\left[\mathbf{u}(\mathbf{x},t)\right]^2}{2c_s^2}\right\} \quad (3)$$

represents the equilibrium distribution function. In equation (3), c_s is the lattice speed of sound, the parameters w_i are a set of weights normalized to unity, $\rho(\mathbf{x},t)$ and $\mathbf{u}(\mathbf{x},t)$ are the fluid density and velocity, respectively. The macroscopic variables are given by the first two moments of the distribution functions:

$$\begin{aligned}\rho(\mathbf{x},t)&=\sum_{i=0}^{N_{pop}-1}f_i(\mathbf{x},t)\\ \rho\mathbf{u}(\mathbf{x},t)&=\sum_{i=0}^{N_{pop}-1}\mathbf{c}_i f_i(\mathbf{x},t)\end{aligned} \quad (4)$$

where N_{pop} denotes the number of discrete velocities. Equation (2) recovers the physics described by the Navier-Stokes equation for an ideal incompressible fluid with the pressure given by:

$$p=\rho c_s^2 \quad (5)$$

and the kinematic viscosity calculated as:

$$\nu=c_s^2\left(\tau_{\mathbf{s}}-\frac{\Delta t_{\mathbf{s}}}{2}\right). \quad (6)$$

B. Unstructured finite-volume formulation for LB method

The approach adopted in this work to numerically solve equation (1), in the unstructured region of the hybrid domain, is a finite-volume scheme of the cell-vertex type based on a space discretization into triangular elements. In Figure 1 a schematic representation of the generic control volume Ω_P around a given node P of the unstructured mesh is provided.

The space-time discretization of the Lattice Boltzmann equation (1) leads to the following expression for each node P of the grid [11, 12, 14]:

$$f_i(P,t+\Delta t_{\mathbf{u}})=f_i(P,t)+\Delta t_{\mathbf{u}}\sum_{k=1}^{K}(\Phi_{ik}-\Xi_{ik}), \quad (7)$$

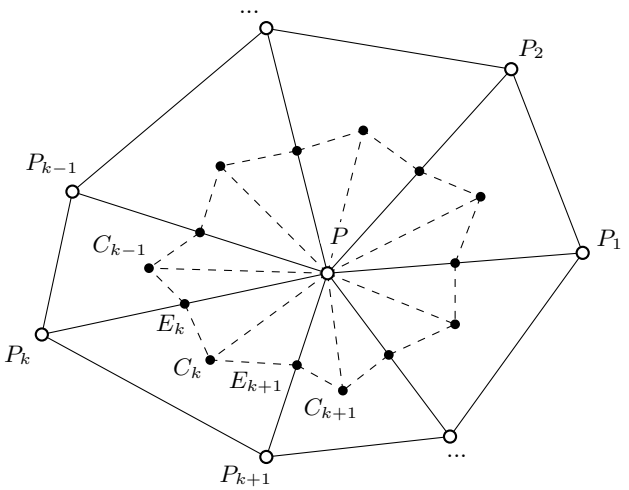

Figure 1: Geometrical layout of the cell-vertex finite volume discretization. The closed dashed-line is the control volume perimeter for the generic node P.

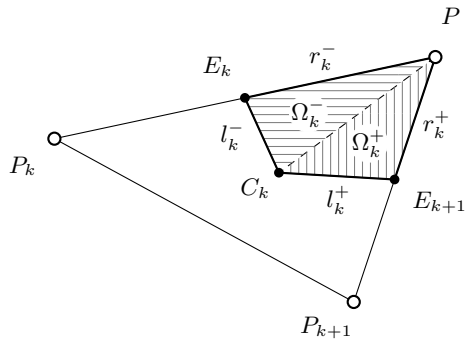

Figure 2: Representation of the k-th portion of the control volume Ω_P. This region is constituted by the sum of two contributions, Ω_k^- and Ω_k^+.

where $\Delta t_{\mathbf{u}}$ is the time step related to the 'unstructured' method. In equation (7), K is the number of elements which share the node P as a common vertex while Φ_{ik} and Ξ_{ik} represents the streaming and collisional fluxes of the i-th population related to the k-th volume, respectively. After manipulation, indicating with $\tau_{\mathbf{u}}$ the 'unstructured' relaxation time, equation (7) can be written in the following general form:

$$f_i(P,t+\Delta t_{\mathbf{u}}) = f_i(P,t) + \Delta t_{\mathbf{u}} \sum_{k=0}^{K'} S_{ik} f_i(P_k,t) - \frac{\Delta t_{\mathbf{u}}}{\tau_{\mathbf{u}}} \sum_{k=0}^{K'} C_{ik}[f_i(P_k,t) - f_i^{eq}(P_k,t)], \quad (8)$$

where $k=0$ denotes the pivotal node P and the summations run over the nodes P_k connected to P. Therefore, K' is equal to K or $K+1$ depending on whether the pivotal node is an internal or a boundary node, respectively. In equation (8) the equilibrium distribution function is defined by equation (3), and S_{ik} and C_{ik} are the streaming matrix and the matrix associated with the collisional term, respectively. The final expressions for such quantities are obtained by application of the following interpolation rules to the integration process:

$$\begin{aligned} f_i(E_k) &= \frac{f_i(P) + f_i(P_k)}{2} \\ f_i(C_k) &= \frac{f_i(P) + f_i(P_k) + f_i(P_{k+1})}{3} \end{aligned} \quad (9)$$

where, with reference to Figures 1 and 2, the point C_k is the centroid of the k-th triangular element and E_k and E_{k+1} are the midpoints of the edges PP_k and PP_{k+1}, respectively.

Thus, for the generic control volume Ω_P of area A_P, the elements of streaming matrix are defined as follows:

$$\begin{aligned} S_{i0} &= \frac{5}{12}\mathbf{c}_i \cdot \sum_{k=1}^{K} \left(\mathbf{l}_k^- + \mathbf{l}_k^+\right) \frac{1}{A_P} + \psi_{B_0}, \\ S_{ik} &= \mathbf{c}_i \cdot \left[\frac{5}{12}\left(\mathbf{l}_k^- + \mathbf{l}_{k-1}^+\right) + \frac{2}{12}\left(\mathbf{l}_k^+ + \mathbf{l}_{k-1}^-\right)\right] \frac{1}{A_P} + \psi_{B_k}, \end{aligned} \quad (10)$$

where $\mathbf{l}_k^-$ and $\mathbf{l}_k^+$ are the vectors normal to the segments E_kC_k and C_kE_{k+1} and which magnitude is equal to their lengths, respectively. Similarly, $\mathbf{l}_{k-1}^-$ and $\mathbf{l}_{k-1}^+$ refer to the segments $E_{k-1}C_{k-1}$ and $C_{k-1}E_k$. In particular, it results $\mathbf{l}_0^+ = \mathbf{l}_K^+$ and $\mathbf{l}_0^- = \mathbf{l}_K^-$ when the pivotal node P is an internal node, while $\mathbf{l}_0^+ = \mathbf{l}_0^- = \mathbf{l}_{K'}^+ = \mathbf{l}_{K'}^- = 0$ for the case of P being a boundary node. Moreover, $\psi_{B_0} = \psi_{B_k} = 0$ if the pivotal node P under consideration is an internal node. The terms ψ_{B_k} represent the contributions due to the external edges ($\mathbf{r}_k^+$ and $\mathbf{r}_k^-$ in Figure 2) occurring when the pivotal node is a boundary node. In this case, in fact, the corresponding control volume do not close up, thus leading to the arising of boundary edges fluxes. In order to deal with such fluxes, we apply the covolume method [14]. Therefore, with reference to Figure 3, where the nodes P_1 and $P_{K'}$ (or P_{K+1}) represent the two boundary nodes adjacent to the pivotal point, it results:

$$\begin{aligned} \psi_{B_0} &= \frac{3}{4}\mathbf{c}_i \cdot \left(\mathbf{r}_1^- + \mathbf{r}_K^+\right) \frac{1}{A_P}, \\ \psi_{B_1} &= \frac{1}{4}\mathbf{c}_i \cdot \mathbf{r}_1^- \frac{1}{A_P}, \\ \psi_{B_{K'}} &= \frac{1}{4}\mathbf{c}_i \cdot \mathbf{r}_K^+ \frac{1}{A_P}. \end{aligned} \quad (11)$$

All the other terms ψ_{B_k} corresponding to any internal node P_k are equal to zero.

Furthermore, the collision matrix is defined as follows:

$$\begin{aligned} C_{i0} &= \frac{11}{18}, \\ C_{ik} &= \left[\frac{5}{18}\left(A_k^- + A_{k-1}^+\right) + \frac{2}{18}\left(A_k^+ + A_{k-1}^-\right)\right] \frac{1}{A_P}, \end{aligned} \quad (12)$$

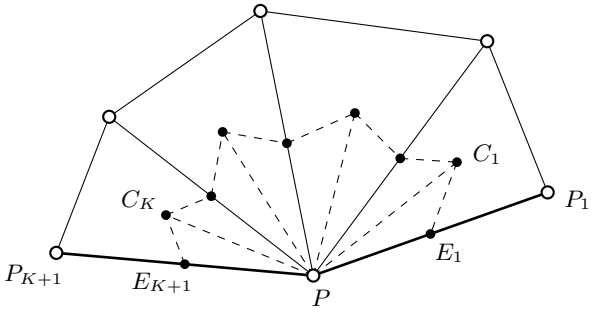

Figure 3: Geometrical layout for boundary elements. The edges $P_{K+1}P$ and PP_1 (thick line) represent a generic boundary of the unstructured mesh.

where A_k^- and A_k^+ are the areas of subregions Ω_k^- and Ω_k^+, respectively, defining the k-th portion of the control volume, as depicted in Figure 2, while A_{k-1}^- and A_{k-1}^+ correspond to the portions Ω_{k-1}^- and Ω_{k-1}^+ of the control volume. In particular, it results $A_0^+ = A_K^+$ and $A_0^- = A_K^-$ when the pivotal node P under consideration is an internal node, while $A_0^+ = A_0^- = A_{K'}^+ = A_{K'}^- = 0$ when P is a boundary node.

Moreover, the following sum rules hold:

$$\sum_{k=0}^{K'} S_{ik} = 0, \quad \sum_{k=0}^{K'} C_{ik} = 1, \quad \forall i. \tag{13}$$

Differently to the standard LB method, the theoretical kinematic viscosity for the unstructured LB implementation does not depends on the choice of the time-step. In fact, it can be proven that, for the model above described, where a first-order time marching scheme is applied, the viscosity is directly proportional to the relaxation time according to the following expression:

$$\nu = c_s^2 \tau_{\mathbf{u}}. \tag{14}$$

A fundamental feature of all the LB finite-volume formulations is a clear separation between the set of discrete speeds and the spatial grid. In other words, the unstructured LB equation is characterized by the *consistency* property, which ensures that all the peculiarities of the standard LB equation retain for the unstructured method as well, in the limit of a uniform lattice. Such evidence leads to the conclusion that the value of the lattice speed of sound, c_s, is the same in both the unstructured and the standard approaches, since the set of discrete speeds is independent from the LB implementation:

$$\delta_{ab} c_s^2 = \sum_{i=0}^{N_{pop}-1} w_i (\mathbf{c}_a)_i (\mathbf{c}_b)_i, \tag{15}$$

where the subscripts a and b denote the spatial coordinates in the lattice space. In this work, the $D2Q9$ model is employed, such that $c_s = 1/\sqrt{3}$, $w_0 = 16/36$, $w_{1,4} = 4/36$ and $w_{5,8} = 1/36$.

C. Hybrid LB formulation

In this section, the principles behind the hybrid method formulation are described.
In order to have a consistent physical flow through the overlapping grid system, many essential requirements need to be addressed.
First, the fluid properties must be the same in the two different grids. Thus, setting the viscosity to be consistent in the entire flow field, results in the following relation between the relaxation times $\tau_{\mathbf{s}}$ and $\tau_{\mathbf{u}}$, characterizing the standard LB and the unstructured LB, respectively:

$$\tau_{\mathbf{u}} = \tau_{\mathbf{s}} - \frac{\Delta t_{\mathbf{s}}}{2}. \tag{16}$$

The defined rule (16) has been obtained by means of expressions (6) and (14). We emphasize that the absence of propagation viscosity $-c_s^2 \Delta t/2$ in the ULBE formulation does not represent a limitation for the viscosity consistency, since the two coupled numerical strategies are equivalent from the macroscopic hydrodynamics simulation point of view [26].
Moreover, both velocity and density must be continuous across the interface region. This implies that the equilibrium distribution functions are the same for the structured and the unstructured systems at interpolation points:

$$f_i^{eq,\mathbf{u}} = f_i^{eq,\mathbf{s}}. \tag{17}$$

Definitions for *interface region* and *interpolation nodes* will be given in section III.
To ensure consistency of the fluid flow, the stress tensor must be continuous along the interfaces. To derive an accurate and suitable relation for the algorithm taking this aspect into account, we first recall the definition of stress tensor for the standard LBGK scheme and for the unstructured formulation, respectively:

$$\Pi_{ab}^{\mathbf{s}} = \left(1 - \frac{\Delta t_{\mathbf{s}}}{2\tau_{\mathbf{s}}}\right) \sum_{i=0}^{N_{pop}-1} (\mathbf{c}_a)_i (\mathbf{c}_b)_i f_i^{neq,\mathbf{s}} \tag{18}$$

$$\Pi_{ab}^{\mathbf{u}} = \sum_{i=0}^{N_{pop}-1} (\mathbf{c}_a)_i (\mathbf{c}_b)_i f_i^{neq,\mathbf{u}} \tag{19}$$

To guarantee the continuity in the stresses, the two tensors (18) and (19) must be the same, thus leading to:

$$f_i^{neq,\mathbf{u}} = \left(1 - \frac{\Delta t_{\mathbf{s}}}{2\tau_{\mathbf{s}}}\right) f_i^{neq,\mathbf{s}}. \tag{20}$$

Equations (17) and (20) represent the starting points of the hybrid scheme routine.
The distribution function field can be decomposed in to two parts:

$$f_i = f_i^{eq} + f_i^{neq}. \tag{21}$$

After applying relation (21) to equations (2) and (8), we can write the post-collision step for both the structured and the unstructured method, respectively, as follows:

$$\tilde{f}_i^{\mathbf{s}} = f_i^{eq,\mathbf{s}} + \frac{\tau_{\mathbf{s}} - \Delta t_{\mathbf{s}}}{\tau_{\mathbf{s}}} f_i^{neq,\mathbf{s}} \tag{22}$$

$$\begin{aligned}\tilde{f}_i^{\mathbf{u}} = f_i^{eq,\mathbf{u}} + f_i^{neq,\mathbf{u}} + \Delta t_{\mathbf{u}} \sum_{k=0}^{K'} S_{ik} \left(f_{ik}^{eq,\mathbf{u}} + f_{ik}^{neq,\mathbf{u}}\right) \\ - \frac{\Delta t_{\mathbf{u}}}{\tau_{\mathbf{u}}} \sum_{k=0}^{K'} C_{ik} f_{ik}^{neq,\mathbf{u}}\end{aligned} \tag{23}$$

By substituting the relations (17) and (20) into the two post-collision equations (22) and (23), respectively, we obtain:

$$\tilde{f}_i^{\mathbf{s}} = f_i^{eq,\mathbf{u}} + \frac{2\left(\tau_{\mathbf{s}} - \Delta t_{\mathbf{s}}\right)}{2\tau_{\mathbf{s}} - \Delta t_{\mathbf{s}}} f_i^{neq,\mathbf{u}} \tag{24}$$

$$\begin{aligned}\tilde{f}_i^{\mathbf{u}} = f_i^{eq,\mathbf{s}} + \left(1 - \frac{\Delta t_{\mathbf{s}}}{2\tau_{\mathbf{s}}}\right) f_i^{neq,\mathbf{s}} \\ + \Delta t_{\mathbf{u}} \sum_{k=0}^{K'} S_{ik} \left[f_{ik}^{eq,\mathbf{s/u}} + \left(1 - \frac{\Delta t_{\mathbf{s}}}{2\tau_{\mathbf{s}}}\right) f_{ik}^{neq,\mathbf{s/u}}\right] \\ - \frac{\Delta t_{\mathbf{u}}}{\tau_{\mathbf{u}}} \left(1 - \frac{\Delta t_{\mathbf{s}}}{2\tau_{\mathbf{s}}}\right) \sum_{k=0}^{K'} C_{ik} f_{ik}^{neq,\mathbf{s/u}}\end{aligned} \tag{25}$$

The two equations (24) and (25) represent the post-collision step for the interpolation nodes, which are responsible of the information exchange between the two grid systems.
In particular, as will be discussed in more detail in the next section, the unstructured interpolation nodes for which equation (25) applies are boundary nodes for the unstructured mesh. Each of these nodes is connected, in turn, with two others unstructured boundary nodes, while the remaining neighbors are unstructured internal nodes. Therefore, the quantities $f_{ik}^{eq,\mathbf{s/u}}$ and $f_{ik}^{neq,\mathbf{s/u}}$ in the summation terms of equation (25) refer to the structured (interpolated) values or to the unstructured values depending on whether the k-th node is an interpolation node or not, respectively.
The particle distribution functions $f_i^{eq,\mathbf{u}}$ and $f_i^{neq,\mathbf{u}}$ of the right-hand side of equation (24) and $f_i^{eq,\mathbf{s}}$ and $f_i^{neq,\mathbf{s}}$ of the right-hand side of equation (25) are evaluated by the interpolation procedure given in the next paragraph. In particular, $f_i^{neq,\mathbf{s}}$ and $f_i^{neq,\mathbf{u}}$, needed to solve equations (24) and (25), correspond to those of equations (22) and (23), respectively.

The two numerical routines need to be solved simultaneously. This means that the characteristic time-steps of the different schemes have to be related to each other. Thus, in order to synchronize the time of the solution, we set:

$$\Delta t_{\mathbf{s}} = n \Delta t_{\mathbf{u}}, \tag{26}$$

where n is a positive integer. In this work, $\Delta t_{\mathbf{s}}$ is set to 1. Moreover, the choice of $\Delta t_{\mathbf{u}}$ is further constrained by the CFL (Courant-Friedrichs-Lewy) stability condition. In fact, due to the explicit time-integration, both the standard LB and the unstructured LB are subjected to such limitation, namely:

$$\Delta t < 2\tau. \tag{27}$$

One more aspect related to the hybrid nature of the method needs to be addressed. It is worth to be noticed that the presence of the unstructured mesh introduces some anisotropy in the space discretization. In order to filter out all the higher than second-order moment contributions due to anisotropy and enhance the stability of the method, a regularization procedure [27, 28] may be necessary in some cases. In the present work, however, we underline that no relevant numerical effects due to anisotropy were observed, thus we did not to implement any strategy along these lines.

III. INTERPOLATION PROCEDURE

The overlapping grid system consists of two components: a structured grid, where the standard LBM is applied, and an unstructured triangular grid, where the finite-volume formulation is solved. The structured grid entirely covers the physical domain, while the unstructured grid is defined only in a certain region of the domain. The two structures overlap and interact to each other along an *interface region*.
The first step of the interpolation procedure consists in the functional classification of the nodal points of each grid. For this purpose, nodes are classified as *discretization*, *interpolation* and *unused* nodes.
To define such classes and then the *interface region*, the following simple procedure is adopted. The unstructured grid *interpolation* nodes are specified in the preprocessing phase. These are defined as all of the nodes belonging to the boundary of the unstructured grid, when this boundary is considered as the *interface* with the structured mesh. All the other nodes constituting the unstructured grid are considered physical *discretization* nodes. Therefore, the structured nodes are initially divided in to two categories, *discretization* and *unused*, depending on whether the node is external or internal, with

respect to a fictitious curve, which is defined within the unstructured grid boundaries. In this paper, we indicate as *interface region* the area included between such fictitious curve and the unstructured *interface* curve, and as *thickness of the interface region*, δ_i, the distance between these two lines. In particular, in the limit case in which these two curves coincide the *thickness of the interface region* is null, namely $\delta_i = 0$. Among the structured *unused* nodes, then, all of them which have at least one physical *discretization* node as neighbor, in any of the eight allowed directions, become an *interpolation* point. Figure 4 depicts an example of overlapping grid system for a generic interface.
Once the whole set of *interpolation* nodes is defined, it is possible to identify the *donor* nodes, namely the nodal points contributing, in terms of macroscopic variables as well as distribution functions, to the computation of the respective values at the *interpolation* points.

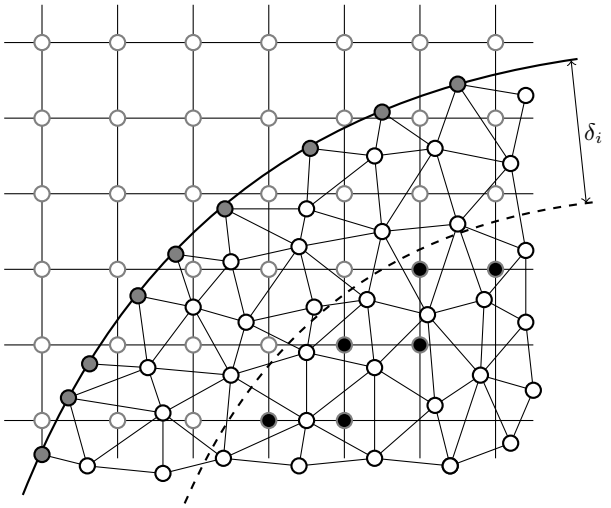

Figure 4: Overlapping grid system. The gray-filled nodes and the black-filled nodes represent the *interpolation* points for the unstructured and the structured grid, respectively. The dashed line is the fictitious line which delimits the *interface region*.

The quantities related to the unstructured interpolation nodes are evaluated by means of a bilinear Lagrange interpolation, which is given by the following formula:

$$\phi(x,y) = \sum_{a=1}^{2}\sum_{b=1}^{2}\left[\phi(x_a,y_b)\mathcal{L}_a(x)\mathcal{L}_b(y)\right]. \qquad (28)$$

In the above, ϕ represents a generic variable, a and b are in this case the indexes along the x and y direction of the structured element, respectively, and:

$$\begin{aligned}\mathcal{L}_a(x) &= \prod_{k=1,k\neq a}^{2}\left(\frac{x_k - x}{x_k - x_a}\right)\\ \mathcal{L}_b(y) &= \prod_{k=1,k\neq b}^{2}\left(\frac{y_k - y}{y_k - y_b}\right),\end{aligned} \qquad (29)$$

are the Lagrange polynomials. Equation (28) is performed over the four nodes constituting the structured element which encloses the unstructured interpolation node under consideration.
As far as the interpolation of the structured nodes concerns, the following scheme, for each interpolation node, is employed:

$$\phi(x,y) = \sum_{k=1}^{3}\phi(x_k,y_k)\beta_k, \qquad (30)$$

where the summation runs over the vertexes of the donor triangular element, namely the element enclosing the structured interpolation node under analysis. The weighted coefficients β_k are computed as the ratio between the relative and the total area of the same element:

$$\beta_k = \frac{A_k}{A_{tot}} \qquad (31)$$

being the relative area A_k defined as the triangular portion of the element which vertexes are the structured interpolation node and the two unstructured nodes of the same element which coordinates indexes are not equal to k. In Figure 5, an illustration for the interpolation scheme is showed.

IV. HYBRID METHOD STRATEGY

The numerical algorithm, at each time interval, can be summarized as follows:

1. After initialization, the *structured* model is solved, with one streaming-collision process carried out for all the discretization nodes.

2. The spatial interpolation of the obtained macroscopic variables is performed by means of equations (28) and the values are stored at the corresponding unstructured interpolation nodes.

3. The *unstructured* model is sub-iterated by applying n times equation (8) to all the discretization nodes. At each sub-iteration the interpolated values for the two components of velocity and density are applied to the scheme as boundary conditions.

4. Once the unstructured routine is completed, the exchange of information in terms of distribution

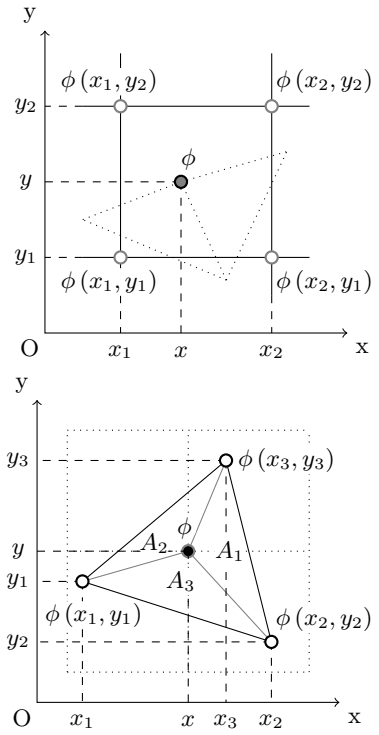

Figure 5: Interpolation schemes representation. On the top: unstructured *interpolation* node in a structured element ; on the bottom: structured *interpolation* node in an unstructured element.

functions takes place. In particular, first the spatial interpolations for $f_i^{eq,\mathbf{s}}$ and $f_i^{neq,\mathbf{s}}$ and for $f_i^{eq,\mathbf{u}}$ and $f_i^{neq,\mathbf{u}}$ are performed by applying equations (28) and (30) at the corresponding interpolation nodes, respectively; finally, the two equations (24) and (25) are applied to all the structured and unstructured interpolation nodes.

The above process is iterated until numerical convergence is reached and the final solution is obtained.
Looking at the given algorithm, we note that, for steady state problems, the structured and the unstructured subroutines can be initialized at two different times. In other words, it is possible to subdivide the simulation in two parts: the first one, where only the structured subroutine is performed for a rough geometry in the uniform spaced domain, and the second one, where also the unstructured subroutine is activated in order to refine the solution. Thus, the proposed numerical algorithm could be modified considering, at the beginning of the simulation, a certain number of sub-iterations for the operation 1, before moving forward to the other steps and repeating the conventional loop. This strategy would significantly speed up the simulation, since the initial transient state, during which the most significant variations in the flow field occur, is solved in a very quick and efficient way by the traditional LBM, while the unstructured model is activated at a later time, with the aim of refining and obtaining the final proper solution.

V. RESULTS AND DISCUSSION

The idea behind this work is to build an overlapping grid system which is constituted by an unstructured mesh covering the boundary layer areas and a structured mesh region which is defined everywhere else in the domain. The two structures interact with each other through the *interface region*, whose minimum thickness is determined through a sensitivity analysis for the specific case considered.
We emphasize that the strategy of covering the entire boundary layer areas by the unstructured grid does not represent a necessary condition, but rather is chosen here as a possible approach. One of the major goals of this work is indeed to verify that the physics of the boundary layer is properly described when the proposed hybrid model is employed.

A. Fluid flow past a circular cylinder

The performance and the efficiency of the proposed overlapping grid system method have been analyzed for the benchmark problem of a uniform flow past a circular cylinder, which numerical and experimental solutions are available in literature.

1. Problem setup

The two-dimensional domain and its main geometrical dimensions are illustrated in Figure 6. The cylinder, of diameter D, is placed symmetrically with respect to bottom and top boundaries of the domain. In particular, following [29], the distance between the center of the cylinder and such lateral surfaces is set to be equal to 10 times the diameter of the cylinder itself, in order to avoid any possible significant effect in the flow field due to the presence of the two boundaries.

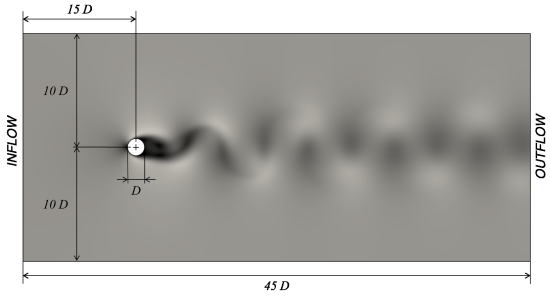

Figure 6: Domain configuration for simulation of fluid flow past a cylinder placed symmetrically in a channel.

A uniform velocity with a zero pressure gradient is set at the inlet, a fixed pressure value and a zero velocity gradient at the outlet, while the no-slip condition is imposed at the cylinder surface. As far as the top and bottom walls of the domain are concerned, we apply an open-boundary condition, namely a zero gradient condition for both velocity and pressure. This condition is implemented, in practice, by simply copying all the distribution functions along the last and the first row of nodes of the domain, respectively, into the corresponding rows of ghost nodes.
The flow problem is simulated for a Reynolds number ranging between 20 and 200, according to the following definition:

$$\mathrm{Re} = \frac{uD}{\nu} \tag{32}$$

being u the main stream velocity.
Concerning the mesh definition, a detail for a generic overlapping grid system is showed in Figure 7. The unstructured grid is constituted by an outer circle area which surrounds the solid body and fully covers the predicted boundary layer thickness.

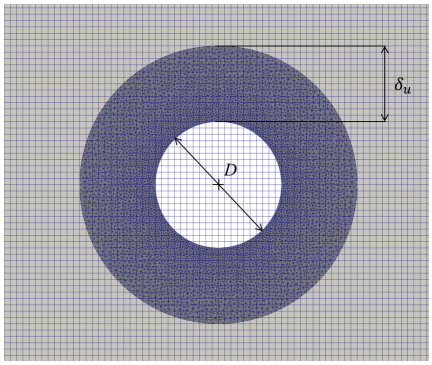

Figure 7: Detail of the hybrid mesh. The domain is fully covered by the structured grid, while an unstructured patch of radial thickness δ_u is defined all around the solid body.

2. *Boundary layer definition*

A preliminary set of simulations is performed in order to estimate the thickness of the boundary layer δ around the cylinder, in the range of Reynolds numbers taken into consideration. Such information will be later employed for the definition of the final configuration of the unstructured mesh. For this preliminary analysis, the cylinder diameter has been chosen to be equal to 20 lattice units and the *thickness of the unstructured mesh* δ_u has been arbitrarily taken equal to 18 lattice units. As far as the *thickness of the interface region*, a value of $\delta_i = \delta_u/2$ has been adopted. After the fully periodic flow solution is reached, the thickness of the boundary layer around the cylinder is evaluated. In particular, we compute δ by considering the distance between a point on the surface of the cylinder at 90 degrees from the frontal stagnation point and that, along the radial direction, where the maximum value of the velocity occurs.
Table I reports the computed numerical values for the non-dimensional parameter $\gamma = \delta/R$, which indicates the ratio between the thickness of the boundary layer δ and the cylinder radius R, corresponding to a point at 90 degrees from the frontal stagnation point, as a function of the Reynolds number.

Table I: Values of the ratio between the boundary layer thickness at 90 degrees from the frontal stagnation point and the cylinder radius, as a function of the Reynolds number.

Re	γ
20	1.53
40	1.03
60	0.81
80	0.67
100	0.58
120	0.52
160	0.46
200	0.38

3. *Sensitivity analysis: effect of unstructured mesh configuration*

A sensitivity analysis has been conducted for the unstructured grid to understand the influence of its configuration on the flow problem. For this purpose, a domain with the same geometry represented in Figure 6 has been kept constant and a cylinder diameter of 20 lattice units has been considered for all the simulations. Both the thickness and the refinement of the unstructured mesh have been varied and, for all the cases, an *interface region thickness* equal to $\delta_u/2$ has been adopted. Two values of the Reynolds number, namely Re = 20 and Re = 80, have been considered for this analysis. In particular, after analyzing the effect due to the variation of δ_u with the level of refinement of the unstructured grid kept constant, a fixed value for the radial thickness has been chosen ($\delta_u = 18$ for Re = 20 and $\delta_u = 8$ for Re = 80) and the number of nodes has been increased progressively. The results, presented in Tables II and III, are expressed in terms of averaged quantities for non-dimensional wake length and drag coefficient. The former is defined as the ratio between the recirculation region in the wake, L, and the cylinder diameter, D, while the latter is defined as follows:

$$C_D = \frac{F_D}{\frac{1}{2}\rho_0 u^2 D}, \tag{33}$$

where F_D is the drag force, which is the horizontal component of the aerodynamic force acting on the solid body, and ρ_0 is the value of the density of the undisturbed fluid flow. In particular, the aerodynamic force has been computed as the sum of two contributions: normal force due to the pressure and shear force due to viscosity. The values for pressure and stress tensor components are locally available and they are evaluated on the nodes defining the body surface by means of equations (5) and (19), respectively. [*SecondReview*] Such a simplification in computing the hydrodynamic forces represents an advantage with respect to traditional LBM. In fact, although interpolation routines are required also in the proposed hybrid method, we note that the interpolations performed in our method are different with respect to those required by traditional LBM. Indeed, the interpolation routines implemented for traditional LB involve the computation of fluid nodes as well as rigid nodes, namely those nodes defining the interior of a solid body. The resulting interpolation schemes are thus characterized by a geometrical complexity which needs to be handled with great care. On the contrary, the interpolation routines required by our algorithm deal with fluid nodes only, whose values are known at each time-step of the simulation, thus leading to easier and less error-prone interpolations. Another disadvantage related to the boundary-fitting concept of traditional LB schemes is that the nice feature of LB of having the stress tensor locally available is partially lost. This property is instead fully preserved by the hybrid method.

Table II: Sensitivity analysis for the unstructured grid: effect of the radial thickness δ_u. Comparison of non-dimensional wake length and drag coefficient for Re = 20 and Re = 80.

	δ_u [l.u.]	L/D	C_D
Re = 20	18	0.955	2.022
	22	0.944	2.019
	26	0.947	2.019
Re = 80	8	1.662	1.370
	11	1.665	1.370
	14	1.664	1.366

Table III: Sensitivity analysis for the unstructured grid: effect of the refinement. Comparison of non-dimensional wake length and drag coefficient for Re = 20 and Re = 80.

	number of nodes	L/D	C_D
Re = 20	7967	0.955	2.022
	10269	0.940	2.018
	14245	0.941	2.019
Re = 80	2978	1.662	1.370
	3733	1.659	1.366
	5092	1.665	1.367

We emphasize that the range of values for δ_u chosen in such analyses differs between the two Reynolds numbers considered, in order to be consistent with the boundary layer thickness, which is lower for higher Reynolds numbers.
The results summarized in Tables II and III clearly show that no substantial differences occur, in terms of both non-dimensional wake length and drag coefficient, when both δ_u and the level of refinement are varied.
In light of these results, the unstructured grid in the following simulations is constituted by an outer circular area whose radial thickness is slightly greater than the computed boundary layer thickness at 90 degrees from the frontal stagnation point. This in order to ensure that the boundary layer region is fully covered by the unstructured grid.

4. *Sensitivity analysis: effect of interface region*

A sensitivity analysis for understanding the effect of the *interface region* and for determining a suitable value for its thickness is presented in this section. With reference to Figure 4, the *interface region thickness* has been varied from 0 to a maximum value given by $\delta_u/2$. All the simulations have been performed with a cylinder diameter of 20 lattice units, for Re = 20 and Re = 80. The results for the different cases are summarized in Table IV.

Table IV: Effect of the *interface region thickness* variation. Comparison of non-dimensional wake length and drag coefficient for Re = 20 and Re = 80.

	δ_i	L/D	C_D
Re = 20	0	0.931	2.026
	$\delta_u/4$	0.943	2.023
	$\delta_u/2$	0.955	2.022
Re = 80	0	1.694	1.362
	$\delta_u/4$	1.662	1.370
	$\delta_u/2$	1.662	1.370

We note that the choice of δ_i has a minor effect, as no significant differences, in terms of both drag coefficient and non-dimensional wake length, are obtained. However, a certain discrepancy occurs when the *thickness of the interface region* is set to zero, especially at Re = 80. A possible explanation for such a behavior can be given considering the interpolation scheme. According to the proposed procedure, when no *interface region* is defined, namely when $\delta_i = 0$, some of the *donor* nodes of one or both grids are *interpolation* nodes at the same time, especially if the size of the two mesh elements are comparable where the two grids interact with each other. As a consequence, the exchange of information at each time interval results to be slightly affected, leading to a weaker connection between the grids.

Although the results for the case of $\delta_i = 0$ can still be considered acceptable, such a limitation can be easily overcome by considering a certain thickness for the *interface region*, as demonstrated by the previous analysis, in such a way to avoid *donor* nodes be classified as *interpolation* nodes at the same time. Thus, on the light of this results, an *interface region thickness* equal to $\delta_u/2$ is adopted hereafter.

5. *Sensitivity analysis: effect of structured mesh configuration*

In order to further validate the analysis conducted so far, a grid-independence study for the structured method has been carried out for Re = 20 and Re = 80. The diameter of the cylinder is varied from $D = 10$ up to $D = 20$ lattice units, while the domain configuration illustrated in Figure 6 has been kept constant. As far as the unstructured mesh concerns, its geometry has been chosen according to the boundary layer thickness criteria described above, assuming the parameter γ to be the same at each value of the cylinder diameter considered, for any given Re. Also for this analysis, the results are compared in terms of mean non-dimensional wake length and mean drag coefficient. They are reported in Table V.

Table V: Sensitivity study for the structured grid: effect of the size of the domain in terms of non-dimensional wake length and drag coefficient.

D [l.u.]	Re = 20		Re = 80	
	L/D	C_D	L/D	C_D
10	0.924	1.998	1.657	1.367
12	0.932	2.012	1.655	1.370
14	0.944	2.011	1.660	1.364
16	0.944	2.011	1.663	1.366
18	0.952	2.019	1.660	1.368
20	0.955	2.022	1.662	1.370

We note that, with the variation of the structured grid size, no significant differences exist for both the normalized length of the recirculation region and the drag coefficient. The analysis confirms the grid-independence of the numerical results.
Table VI shows a comparison for the non-dimensional recirculation region among the obtained values for the case of a diameter equal to 20 lattice units and values available in literature. The results are in line with the previous works [30–36].

6. *Final results and validation*

With all the parameters of the overlapping grid system defined, a set of simulations with a Reynolds number ranging between 20 and 200 has been performed. The cylinder diameter has been taken equal to 20 lattice units. Figure 8 shows the instantaneous velocity and pressure fields for Re = 40, 100 and 200, respectively.

Table VI: Obtained values for the non-dimensional wake length L/D, for Re = 20 and Re = 80. The results are compared with literature data.

	Re	L/D
X. He and G.Doolen [30]	20	0.921
S.C.R. Dennis and G. Chang [31]		0.94
Z. Guo et al. [32]		0.934
R. Mei and W. Shyy [33]		0.902
G. Eitel-Amor et al. [34]		0.920
present study		0.955
J. Park et al. [35]	80	1.66
L. Qu et al. [36]		1.67
present study		1.662

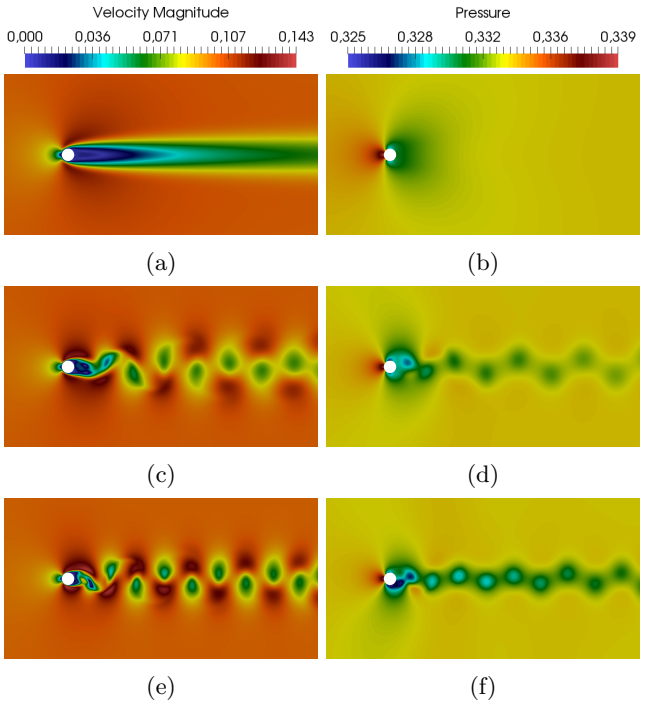

Figure 8: Instantaneous velocity and pressure fields: (a),(b): Re = 40 ; (c),(d): Re = 100 ; (e),(f): Re = 200

As expected, for Re = 40 the laminar steady regime solution is obtained, while, for higher values of Re, the laminar vortex shedding phenomenon can be clearly observed. This is consistent with the experimental and numerical predictions available in literature, which identify a critical Re between 45 and 50, beyond which the recirculation region develops instabilities and the unsteady flow separation on the cylinder surface leads to the formation of the *Karman vortex street*. Figure 9 shows a detail of the instantaneous shear stress field, in terms of its components Π_{aa}, Π_{ab} and Π_{bb}, respectively, for Re = 80.

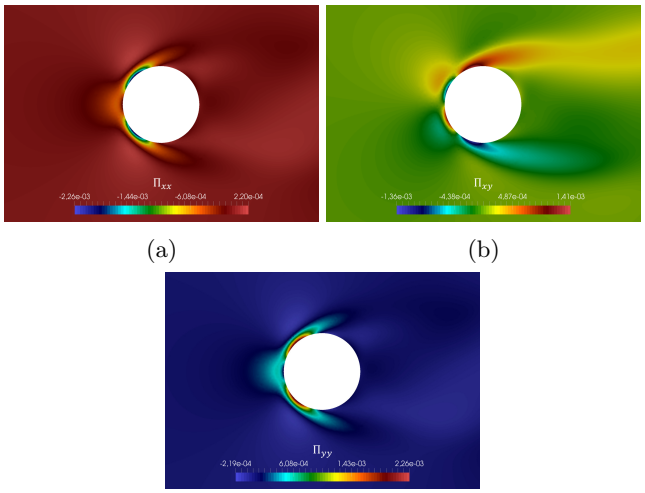

Figure 9: Instantaneous shear stress field at Re = 80: (a) Π_{aa} ; (b) Π_{ab} ; (c) Π_{bb}

As it possible to notice, no discontinuity at all, for all the quantities analyzed, is observed.
Table VII lists the average values obtained for the drag coefficient as a function of Reynolds number.

Table VII: Obtained values for the average drag coefficient as a function of the Reynolds number.

Re	C_D
20	2.022
40	1.512
60	1.404
80	1.370
100	1.348
120	1.329
160	1.329
200	1.343

Figure 10 reports the drag coefficient as a function of the Reynolds number compared to literature data, confirming that our results are in excellent agreement with those of previous experimental and numerical studies [11, 35, 37–40].

Figure 11 shows the evolution in time of the drag coefficient for two different values of Re. Similar trends are obtained for all the other values considered.

We observe that the solution stabilizes within 80000 iterations even in the most critical case (Re = 200), with the C_D oscillating around a constant value. However, for Re lower than the critical value, with the increasing of iterations the drag coefficient converges to a fairly constant value, while for higher Re we observe a time-periodic function. For Re = 200 instead, which is representative of a wake-transition regime, the time-periodic trend appears to be slightly altered, due to the occurring of intermittent low-frequency irregularities in the velocity fluctuations downstream of the cylinder [41].

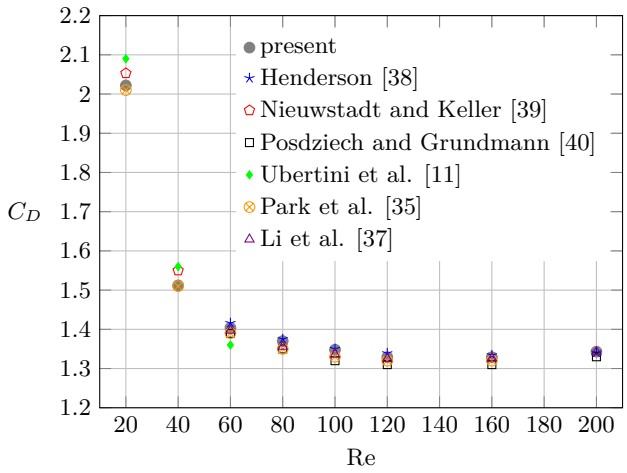

Figure 10: Drag coefficient as a function of the Reynolds number. The results are compared with literature data.

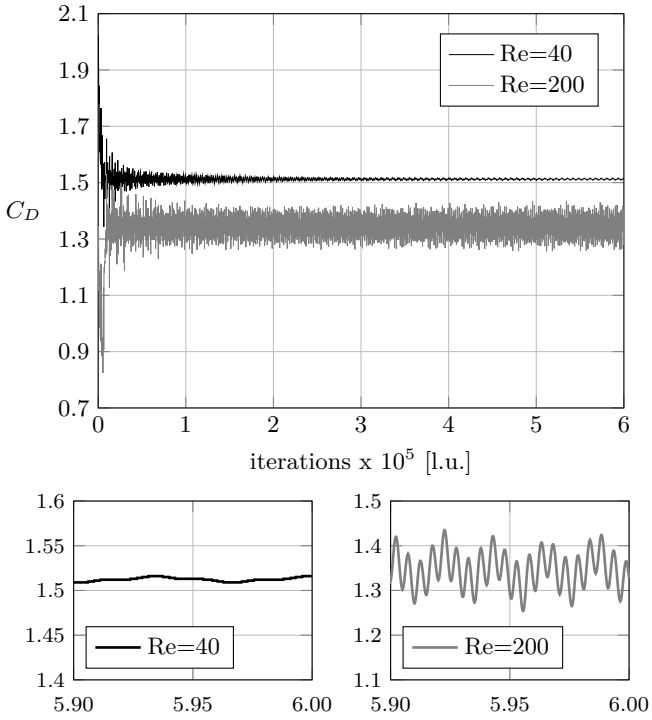

Figure 11: Variation of drag coefficient with time for Re = 40 and Re = 200. The top figure shows the trend between 0 and 600000 iterations; the bottom figures show a detail for the drag coefficient evolution for Re = 40 (left) and Re = 200 (right).

Figure 12 shows the time-averaged pressure coefficient C_p, defined as

$$C_p = \frac{p - p_0}{\frac{1}{2}\rho_0 u^2} \tag{34}$$

along the cylinder surface for all the cases studied. In the above relation p is the local pressure while p_0 represents the free-stream pressure. Figure 13 reports a comparison with reference values available in literature, for two Reynolds numbers.

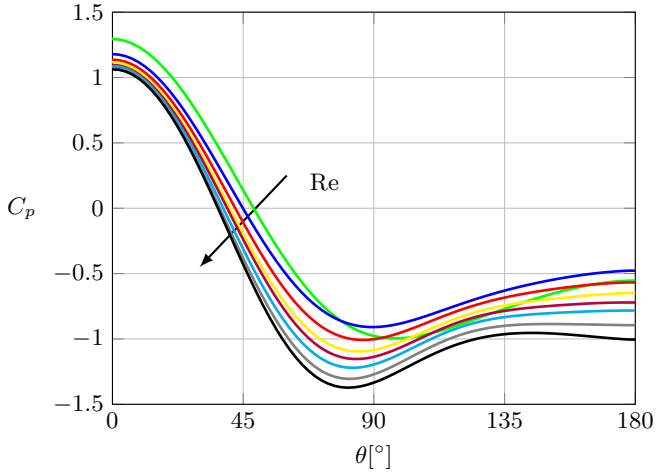

Figure 12: Time-averaged pressure coefficient along the cylinder surface for Re = 20, 40, 60, 80, 100, 120, 160, 200. $\theta = 0^\circ$ and $\theta = 180^\circ$ correspond to the front and the rear stagnation points, respectively.

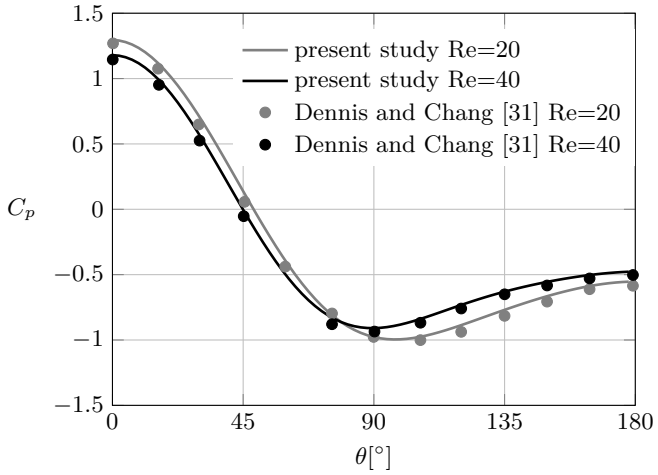

Figure 13: Pressure coefficient trend from the front ($\theta = 0^\circ$) to the rear ($\theta = 180^\circ$) stagnation point. The results for Re = 20 and Re = 40 are compared with reference values.

Further, Figures 14 illustrates the variation of the base suction coefficient, C_{pb}, which is defined as the pressure coefficient at the rear stagnation point of the cylinder, as a function of the Reynolds number. The base pressure parameter is an indicator of the flow regime, since its sensitiveness to the changes in flow instabilities over the Reynolds number.

The obtained trend for the base suction coefficient corresponds to the typical one (see also [41]). The value of $-C_{pb}$ decreases by increasing Re until a critical value is reached. Above this limit the flow becomes unsteady and, in the range of Re which is characterized by laminar vortex shedding, the base suction coefficient has opposite trend. In literature, the upper limit of the laminar shedding regime has a significant spread. Williamson [41] reports a range of values for this particular Re between 140 and 194. Beyond this critical value a wake-transition regime occurs causing a discontinuity in the $-C_{pb}$ trend. The reason behind the difference in results, shown in Figure 14, between our values and those obtained experimentally by Williamson and Roshko [42] can be attributed to this fact.

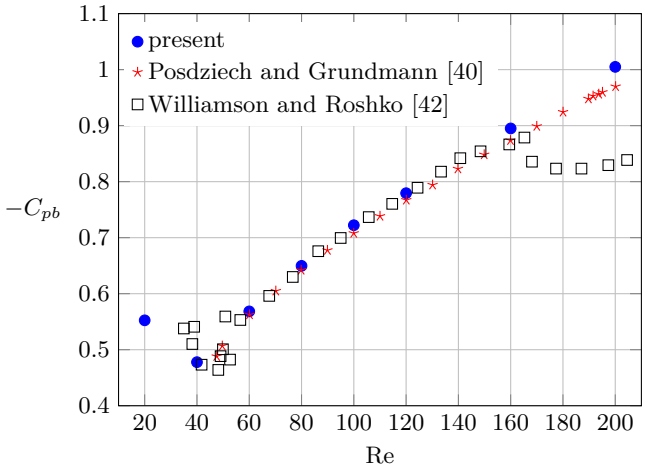

Figure 14: Base suction coefficient as a function of the Reynolds number. The results are compared with literature data.

Finally, the time-mean separation angle is presented in Figure 15. Such parameter has been evaluated as the point on the cylinder surface where the shear stress vanishes.

Figures 13, 14 and 15 clearly show that the analyzed parameters are in good agreement with the correspondent values available in literature.

VI. NUMERICAL PERFORMANCE ANALYSIS

The proposed hybrid method is here compared with a standard LBGK implementation, for the case of a two-dimensional flow past a circular cylinder, and its performance is measured in order to evaluate the effectiveness of the method. For the comparison, the same LBGK scheme used for the solution of the structured grid in the hybrid algorithm has been employed. For this case, the domain has been taken to be the same of the one described in Figure 6 and the number of nodes (consequent to the cylinder diameter length definition) has been chosen according the minimum distance between two lattice nodes occurring in the overlapping system grids. Such

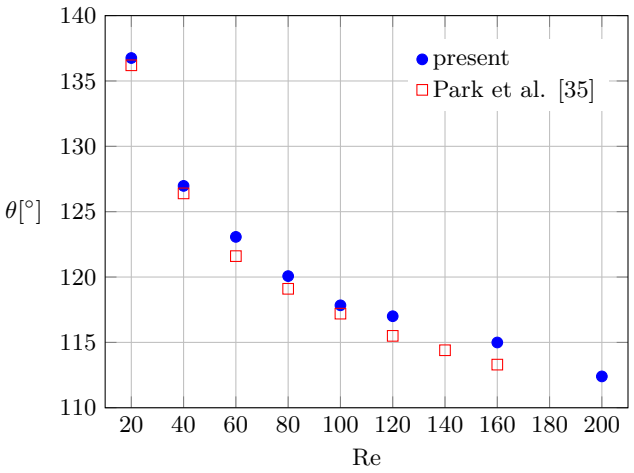

Figure 15: Separation angle as a function of Reynolds number. The results are compared with literature data.

dimension is 0.4 lattice units for all the meshes employed in the final set of simulations. In particular, this length corresponds to the average distance between two nodes in the unstructured grid at the boundary of the solid body. Thus, considering that a cylinder diameter of 20 lattice units is employed for the overlapping grid system solution, a diameter equal to 50 lattice units must be adopted for the LBGK method in order to have a similar mesh resolution in proximity of the body.

A set of simulations for the same values of the Reynolds number considered in the former analysis has been performed with the standard LBGK approach. The explicit nature of this method leads to the onset of instabilities which generate the unsteady flow behavior when the Reynolds number is increased above the critical value. Some of the authors investigated the effects due to the choice of the numerical scheme adopted. A detailed discussion is available in [43].

As far as the boundary conditions are concerned, the ones used in the hybrid method have been set in the present analysis as well. In particular, the no-slip condition at cylinder surface is imposed, in this case, through a second-order bounce-back condition. Moreover, for all the cases, the same Mach number (Ma = 0.17) for the inlet velocity used in the hybrid scheme has been adopted. Tables VIII and IX report a comparison between the results, expressed in terms of drag coefficient, pressure base coefficient and separation angle, obtained by the hybrid method and the standard LBGK method.

[*SecondReview*] Although the standard LBGK seems to slightly underestimate the drag coefficient, we note that the two methods lead to very comparable results.

Figure 16 shows a visualization for the hybrid mesh in comparison with the uniform structured one. From Figure 16, one of the key advantages of HLBM over standard LBGK is clearly appreciated: the coexistence of an unstructured and a structured grid allows high definition of the body surface while keeping a coarser discretization

Table VIII: Drag coefficient obtained by HLBM and LBGK for Reynolds number between 20 and 200. The range of values found in the literature ([11, 35, 37–40]) is reported, for each Reynolds number, as a reference.

Re	C_D		
	HLBM	LBGK	References
20	2.022	1.909	2.010 – 2.090
40	1.512	1.433	1.510 – 1.560
60	1.404	1.333	1.360 – 1.416
80	1.370	1.297	1.350 – 1.375
100	1.348	1.279	1.320 – 1.350
120	1.329	1.272	1.310 – 1.339
160	1.329	1.279	1.310 – 1.334
200	1.343	1.296	1.330 – 1.342

Table IX: Comparison between HLBM and LBGK for Reynolds number between 20 and 200. Values for pressure base coefficient and separation angle are reported.

Re	$-C_{pb}$		$\theta[^\circ]$	
	HLBM	LBGK	HLBM	LBGK
20	0.552	0.553	136.76	139.18
40	0.478	0.488	126.97	129.50
60	0.568	0.577	123.07	125.75
80	0.650	0.661	120.07	123.57
100	0.722	0.730	117.84	121.92
120	0.779	0.792	117.00	120.64
160	0.895	0.907	114.99	119.25
200	1.005	1.003	112.40	118.50

everywhere else in the domain; although with an uniform spaced mesh it is possible to achieve similar resolution by using a larger number of nodes within the domain, the geometry profile is, in this case, still described by means of a stepped surface.

In order to quantify the differences, in terms of numerical performances, between the hybrid scheme and the equivalent standard uniform spaced scheme, the following speedup (gain) coefficient has been defined:

$$G = \frac{T_{\mathbf{h}}}{T_{\mathbf{eq}}}, \tag{35}$$

where $T_{\mathbf{h}}$ and $T_{\mathbf{eq}}$ represent the wall-clock times, required by a single algorithm iteration, for the hybrid and for the equivalent structured methods, respectively.

By definition $G < 1$ denotes the regime where the hybrid method runs faster than the standard LBGK.

The wall-clock time $T_{\mathbf{h}}$ is defined as the sum of two contributions:

$$T_{\mathbf{h}} = T_{\mathbf{s}} + T_{\mathbf{u}}, \tag{36}$$

where the execution CPU-time required to complete the structured and the unstructured subroutines, respec-

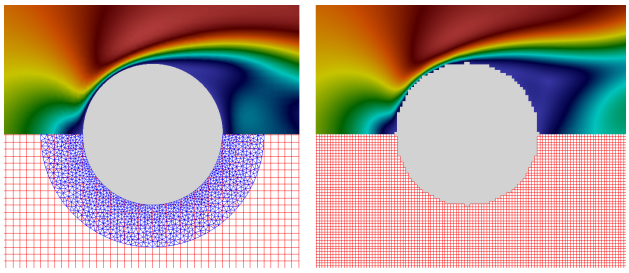

Figure 16: Graphic visualization of the hybrid mesh (left) in comparison with the uniform structured one (right).

tively, are:

$$T_{\mathbf{s}} = \frac{N_{\mathbf{s}}}{S_{\mathbf{s}}}, \qquad T_{\mathbf{u}} = \frac{N_{\mathbf{u}}}{S_{\mathbf{u}}}, \tag{37}$$

In equations (37), $N_{\mathbf{s}}$ and $N_{\mathbf{u}}$ represent the numbers of nodes associated with the structured and unstructured subroutines, respectively, while $S_{\mathbf{s}}$ and $S_{\mathbf{u}}$ refer to the corresponding overall processing speeds. $S_{\mathbf{s}}$ and $S_{\mathbf{u}}$ are measured in *Millions of Lattice Updates per Second* (MLUPS) and they include the computational contributions due to the handshaking process. The wall-clock time for the equivalent structured scheme is defined as follows:

$$T_{\mathbf{eq}} = \frac{N_{\mathbf{eq}}}{S_{\mathbf{eq}}}, \tag{38}$$

where $N_{\mathbf{eq}}$ represents the equivalent number of nodes for the standard LBGK method in order to have a similar accuracy with the HLBM and $S_{\mathbf{eq}}$ is the processing speed characterizing the equivalent structured algorithm.
In order to find a general expression for the parameter G and to emphasize the role of the main factors contributing to the HLBM computational performance, we introduce the following non-dimensional groups:

$$\chi = \frac{N_{\mathbf{u}}}{N_{\mathbf{s}}}, \quad g = \frac{N_{\mathbf{eq}}}{N_{\mathbf{s}}}, \quad s = \frac{S_{\mathbf{s}}}{S_{\mathbf{u}}}, \quad s_{eq} = \frac{S_{\mathbf{eq}}}{S_{\mathbf{s}}}, \tag{39}$$

Thus, after manipulation, the speedup indicator can be expressed as follows:

$$G = \frac{(1+\chi s)s_{eq}}{g} \tag{40}$$

From equation (40), it can be noticed that the computational efficiency gain associated with the HLBM is controlled by the factor g, which represents a measure of the computational saving in terms of number of structured nodes required. The value of g is greater than 1 and such effect is due to the presence of the unstructured component, which can be regarded as a sort of "computational catalyst" of the hybrid method. The effectiveness of the unstructured computational catalyst is described by the parameter χ. This quantity represents the amount of unstructured nodes required with respect to the number of structured nodes and it should be kept as small as possible in order to enhance the numerical performance of the HLBM. On the other hand, the numerical efficiency of the hybrid scheme is penalized by the factors s and s_{eq}. The former quantity represents the overhead due to the lower processing speed associated with the unstructured subroutine with respect to the structured one. The latter corresponds instead to the overhead due to the lower processing speed of the structured subroutine with respect to the equivalent structured method. In general, this second effect is due to the relatively higher number of operations required by the coupling process for the structured subroutine of the hybrid method. However, the interpolation procedure consists of few operations involving only a minority of nodes with respect to the total amount. For this reason, the computational time required by the coupling process in the structured subroutine is extremely small and it can be considered negligible with respect to the overall wall-clock time required by this subroutine. This leads to the conclusion that:

$$s_{eq} \simeq 1, \tag{41}$$

as the processing speeds of structured subroutine and equivalent structured algorithm are nearly the same. A similar consideration applies to the unstructured subroutine of the hybrid scheme. In fact, also in this case, the wall-clock time due to the coupling process is negligible with respect to the total computational time required by the unstructured subroutine. Therefore, the specific processing speed of the unstructured subroutine, which is defined as the processing speed associated with one single iteration of the unstructured routine, can be expressed as:

$$S'_{\mathbf{u}} \simeq S_{\mathbf{u}} n, \tag{42}$$

where n is the number of sub-iterations required within the hybrid scheme as defined in equation (26). By introducing the following parameter:

$$s' = \frac{S_{\mathbf{s}}}{S'_{\mathbf{u}}}, \tag{43}$$

and applying equations (41) and (43), the computational performance indicator G can be expressed as:

$$G = \frac{1+\chi s' n}{g} \tag{44}$$

The parameter s' expresses the differences of cost per computational node and time-step, in terms of processing speed required, between the standard uniform spaced LBGK method and the unstructured method. Its value typically ranges between 3 and 5 [11] as found also in the present analysis.
The parametric study on the code performance was then conducted by considering unstructured meshes of different sizes (the entire set of meshes employed for obtaining the final results for the fluid dynamic problem analyzed in this study) and by varying the number of sub-iterations for the unstructured subroutine. All the tests were performed on a workstation, using a single core, which features are: *CPU: Intel Core i5-2450M, RAM: DDR3, 667 MHz, timings 9-9-9-24*. The processing speed for the equivalent standard LBGK method and for the structured subroutine, $S_{\mathbf{eq}}$ and $S_{\mathbf{s}}$, respectively, were evaluated to be both equal to 10.5 MLUPS while for the unstructured algorithm employed in the hybrid scheme the value of $S'_{\mathbf{u}}$ ranges between 2.2 and 3.6 MLUPS, depending on the mesh definition. The reported values for the processing speeds were computed considering the average on three runs of 500 iterations each. Since the variability of the results between the tests was found to be negligible, this number of runs was considered sufficient.
For the present test case as an example in this comparison, the numbers of nodes required by the equivalent standard LBGK method to have a similar resolution around the body is about 6 times greater than the total number of nodes employed by the HLBM. In particular, we find $g \simeq 6.2$.
The histogram representation in Figure 17 shows the trend of the numerical performances of the hybrid method, in terms of speedup indicator G as a function of the parameter χ and the required number of sub-iterations n.

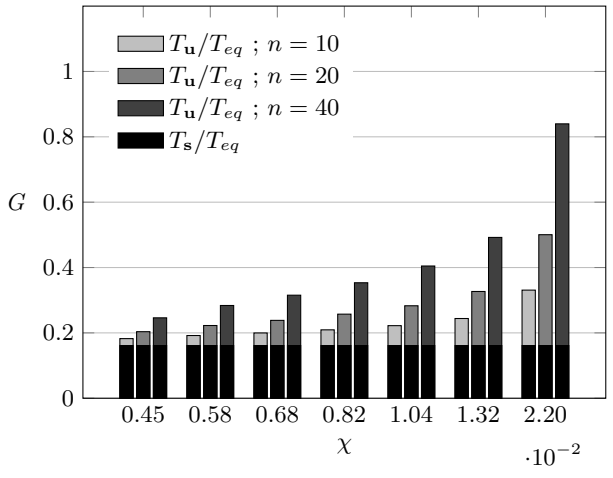

Figure 17: Speedup indicator G for $g = 6.2$ and for different values of the parameter χ. The total non-dimensional execution time is constituted by two contributions, related to the structured and the unstructured subroutine, respectively.

The results presented in Figure 17 indicate that, in all the numerical tests, the hybrid method is faster than the equivalent uniform spaced one, in terms of total execution CPU-time required to solve the same number of iterations, since the obtained values of G are always lower than 1. The hybrid scheme is more efficient than the equivalent structured one even for relatively high values of χ (which corresponds to high percentage of unstructured nodes) and relatively high numbers of sub-iterations. In particular, it is also possible to understand the influence of the unstructured subroutine, whose contribution, in terms of execution CPU-time, represents the most significant share only when the percentage of unstructured nodes exceed about the 2% of the number of structured nodes and for relatively high values of n.
With reference to equation (44), the obtained results confirm the need of limiting to a reasonable value the parameter χ, which corresponds to the percentage number of unstructured nodes, in order to increase the performance of the hybrid method. The same applies to the number of sub-iterations n for the unstructured subroutine. This result highlights that, in general, the hybrid discretization offers a twofold benefit with respect to the structured uniform lattice spacing: an improvement in computational efficiency and a more precise definition of the solid body geometry profile.
The comparison between the two methods has been performed for the specific case of $g = 6.2$, as an illustrative example. However, it is important to note that the refinement of the unstructured mesh is not subject to strict limitations. This means that, in theory, the hybrid method allows an increasing of the mesh resolution in proximity of the body without affecting its numerical performance. It is therefore possible to state that, in general, the efficiency of the proposed method is much higher than the one corresponding to the traditional structured scheme, and the differences in terms of numerical performances increase with the increasing of the level of refinement.
Moreover, the presence of the unstructured mesh allows a flexible and progressive transition to different levels of refinement within the space domain. This feature makes the HLBM much more adaptable to complex geometries with respect to the conventional LB refinement methods currently available in literature.
Besides the numerical efficiency, another significant advantage of the hybrid method is that the scheme does not require any interpolation routine to compute the values of the variables of interest on the real boundary of the solid body, differently from the standard LBM. The lattice nodes definition of the HLBM is naturally adapted to the geometry of the solid bodies, thus high accuracy is achieved in the evaluation of flow variables, forces and moments at solid walls.

VII. CONCLUSIONS

An Hybrid Lattice Boltzmann model has been proposed in this work and its capabilities explored through the analysis of the benchmark problem of the two-dimensional flow past a circular cylinder. The study demonstrates the robustness and the efficiency of the new method. In particular, the HLBM is found to be accurate in the prediction of the boundary layer physics and in the computation of the forces acting on the solid body. In fact, a local refinement around the body is realized by the presence of the unstructured grid and, since the nodal unknowns are placed exactly on the boundary of the object, no interpolation routine is needed to compute the fluid dynamic variables in that region. Moreover, the unstructured grid resolution in proximity of the body allows the fluid domain to be covered by a significant less number of lattice nodes, with respect to the case of a standard uniform spaced LB scheme, which results in a substantial enhancement of the numerical performance. Despite some complexity due to the presence of the unstructured routine, the proposed hybrid method results in a model that is still relatively easy to implement and parallelize. In fact, the computation of each node in the unstructured scheme only involves information within local neighborhoods. These features, together with the possibility of merging the hybrid procedure with a traditional grid refinement model, make the method suitable to handle complex geometries, to solve turbulent flows as well as to deal with multi-scale problems.

[*SecondReview*] Summarizing, the proposed hybrid method could bring the following practical advantages with respect to traditional LBM: i) the possibility of handling more complex geometries, due to the adaptivity of the mesh system and a more precise definition of the solid body geometry profile; ii) high accuracy near the solid walls, thanks to the capability of refining the discretized domain in a very flexible way; iii) the fact that the stress tensor is locally available on the nodes of the computational domain, such that hydrodynamic forces on solid bodies can be calculated without any boundary-fitting procedure. Moreover, the enhanced near-wall resolution is instrumental to the implementation of multi-scale schemes, coupling LB to more microscopic treatments, such as Direct Simulation Monte Carlo (DSMC) or Molecular dynamics (MD).

[1] C. K. Aidun and J. R. Clausen, Annu. Rev. Fluid Mech. **42**, 439 (2010).
[2] S. Succi, *The Lattice Boltzmann Equation for Fluid Dynamics and Beyond* (Clarendon Press, 2001).
[3] S. Chen and G. D. Doolen, Annu. Rev. Fluid Mech. **30**, 329 (1998).
[4] S. Succi, EPL **109**, 50001 (2015).
[5] R. Benzi, S. Succi, and M. Vergassola, Phys. Rep. **222**, 145 (1992).
[6] F. Higuera and S. Succi, Europhys. Lett. **8**, 517 (1989).
[7] F. Nannelli and S. Succi, J. Stat. Phys. **68**, 401 (1992).
[8] D. Kandhai, W. Soll, S. Chen, A.Hoekstra, and P. Sloot, Comput. Phys. Commun. **129**, 100 (2000).
[9] G. Peng, H. Xi, C. Duncan, and S. Chou, Phys. Rev. E **58**, R4124 (1998).
[10] H. Xi, G. Peng, and S. Chou, Phys. Rev. E **59**, 6202 (1999).
[11] S. Ubertini, S. Succi, and G. Bella, Phil. Trans. R. Soc. Lond. A **362**, 1763 (2004).
[12] S. Ubertini and S. Succi, Commun. Comput. Phys. **3**, 342 (2007).
[13] S. Ubertini, G. Bella, and S. Succi, Math. Comp. Sim. **72**, 237 (2006).
[14] S. Ubertini, G. Bella, and S. Succi, Phys. Rev. E **68**, 016701 (2003).
[15] T. Lee and C. Lin, J. Comp. Physics **171**, 336 (2001).
[16] T. Lee and C. Lin, J. Comp. Physics **185**, 445 (2003).
[17] M. Min and T. Lee, J. Comp. Physics **230**, 245 (2011).
[18] S. Patel and T. Lee, J. Comp. Physics **327**, 799 (2016).
[19] O. Filippova and D. Hanel, J. Comp. Physics **147**, 219 (1998).
[20] O. Filippova and D. Hanel, J. Comp. Physics **165**, 407 (2000).
[21] C. Lin and Y. Lai, Phys. Rev. E **62**, 2219 (2000).
[22] D. Yu, R. Mei, and W. Shyy, Int. J. Numer. Meth. Fluids **39**, 99 (2002).
[23] A. Dupuis and B. Chopard, Phys. Rev. E **67**, 066707 (2003).
[24] H. Chen, O. Filippova, J. Hoch, K. Molvig, R. Shock, C. Teixeira, and R. Zhang, Physica A **362**, 158 (2006).
[25] N. Rossi, S. Ubertini, G. Bella, and S. Succi, Int. J. Numer. Meth. Fluids **49**, 619 (2005).
[26] S. Ubertini, P. Asinari, and S. Succi, Phys. Rev. E **81**, 016311 (2010).
[27] J. Latt and B. Chopard, Math. Comput. Simul. **72**, 165 (2006).
[28] R. Zhang, X. Shan, and H. Chen, Phys. Rev. E **74**, 046703 (2006).
[29] M. Behr, D. Hastreiter, S. Mittal, and T. Tezduyar, Comput. Methods in Appl.Mech.Eng **123**, 309 (1995).
[30] X. He and G. Doolen, J. Comp. Physics **134**, 306 (1997).
[31] S. Dennis and G. Chang, J. Fluid Mech. **42**, 471–489 (1970).
[32] Z. Guo, B. Shi, and N. Wang, J. Comp. Physics **165**, 288 (2000).
[33] R. Mei and W. Shyy, J. Comp. Physics **143**, 426 (1998).
[34] G. Amor, M. Meinke, and W. Schroder, 20th AIAA Computational Fluid Dynamics Conference (2011), 10.2514/6.2011-3398.
[35] J. Park, K. Kwon, and H. Choi, KSME Int. J. **12**, 1200 (1998).
[36] L. Qu, C. Norberg, L. Davidson, and S. Peng, J. Fluid. Struct. **39**, 347 (2013).
[37] Y. Li, R. Zhang, R. Shock, and H. Chen, Eur. Phys. J. Special Topics **171**, 91 (2009).
[38] R. Henderson, Phys. Fluids **7**, 2102 (1995).

[39] F. Nieuwstadt and H. B. Keller, Comput. Fluids **1**, 59 (1973).
[40] O. Posdziech and R. Grundmann, Theoret. Comput. Fluid Dynamics **15**, 121 (2001).
[41] C. Williamson, Annu. Rev. Fluid. Mech. **28**, 477 (1996).
[42] C. Williamson and A. Roshko, Z. Flugw. Weltraumf **14**, 38 (1990).
[43] G. Di Ilio, D. Chiappini, and G. Bella, Int. J. Mod. Phys. C **27**, 1650139 (2016).